scientific reports

Check for updates

OPEN

Cross-seasonal influence of China Coastal Current water on spring carbonate system in the northern South China Sea

Shiping Lei[1,2], Yi Yang[1], Dezhi Bu[1], Xianghui Guo[1,3]✉, Yan Li[1], Kuanbo Zhou[1], Jin-Yu Terence Yang[1] & Zhongyong Gao[4]

This study investigates the carbonate system in the northern South China Sea shelf off the Pearl River estuary during the spring of 2023. Contrary to the typical distribution pattern observed in river-dominated coast where dissolved inorganic carbon (DIC) increases offshore, field observations revealed higher DIC in inshore waters (> 1980 μmol kg^{-1}) than in offshore seawaters (< 1970 μmol kg^{-1}), with DIC in the coastal zone being 20.9±8.8 μmol kg^{-1} higher than that offshore. An end-member mixing model indicated that the high DIC coastal water was primarily attributed to mixing with the remnant high-DIC southward winter China Coastal Current water. In addition, biological processes and air-sea CO_2 exchange also played important roles. Two representative regions were examined: the inshore high-DIC region and the offshore low-DIC region. In the inshore high-DIC region, biological processes and air-sea CO_2 exchange increased DIC by 11.6 ± 3.0 (relative to air-sea CO_2 equilibrium) and 1.1 ± 7.0 μmol kg^{-1} (relative to conservative mixing), respectively. In the offshore low-DIC region, biological processes decreased DIC by 5.1 ± 3.5 μmol kg^{-1}, whereas air-sea CO_2 exchange increased DIC by 9.9 ± 2.8 μmol kg^{-1}. Overall, this study highlights the dominant role of the cross-seasonal influence of the remnant water of the coastal current, as well as the secondary but significant contributions of biological activity and air-sea CO_2 exchange to the DIC distribution in coastal regions.

Keywords Pearl River estuary, Northern South China Sea coast, Dissolved inorganic carbon, Water mass mixing, Biogeochemical processes, Air-sea CO_2 exchange

Estuarine-coastal zones are transitional regions between the land and sea, connecting rivers and oceans. During the mixing of river water and seawater, biogeochemical parameters in estuaries (such as nutrients, dissolved inorganic carbon and organic carbon) generally exhibit strong gradients[1,2]. Although coastal regions (continental shelves) account for less than 10% of the global ocean area[3], they contribute approximately 30% of global ocean primary productivity, 10%–25% of marine carbon sinks, and up to 80% of global ocean organic carbon burial[4–6]. Consequently, estuarine carbon cycling represents a crucial component of the global ocean carbon cycle[2]. Key physical and biogeochemical processes regulating dissolved inorganic carbon (DIC) in estuarine-coastal systems include riverine input, upwelling, coastal currents, biological activity, air-sea CO_2 exchange, carbonate calcium precipitation/dissolution and water-sediment interface exchange, etc.[5,7]. These processes interact complexly to jointly regulate the spatiotemporal distribution of DIC.

The northern South China Sea (NSCS) shelf is a tropical marginal sea of the Northwestern Pacific. Its unique geographical setting and complex hydrodynamic environment characterized, for example, by physical mixing of Pearl River discharge and coastal upwelling water, make it a representative region for investigating the coupling mechanisms between physical and biogeochemical processes[8,9]. Under the strong influence of the northeast monsoon in winter, the China Coastal Current (CCC) water primarily originating from the East China Sea and even the Yellow Sea characterized by low temperature, low salinity, high concentrations of nutrients, DIC and total alkalinity (TA), reaches the NSCS shelf and influences its biogeochemical processes[10–15].

[1]State Key Laboratory of Marine Environmental Science, College of Ocean and Earth Sciences, Xiamen University, Xiamen 361102, China. [2]Ningde Ocean Innovation Center, Ningde 352100, China. [3]Fujian Provincial Key Laboratory for Coastal Ecology and Environmental Studies, Xiamen University, Xiamen 361102, China. [4]Third Institute of Oceanography, Ministry of Natural Resources, Xiamen 361005, China. ✉email: xhguo@xmu.edu.cn

Han et al.[11] estimated that the flux of dissolved inorganic nitrogen (DIN) transported by the CCC to the NSCS during winter is approximately $(8.0 \pm 5.7)\times10^8$ g. Meng et al.[16] revealed that the dissolved organic carbon (DOC) flux transported by the CCC to the NSCS is approximately $(82 \pm 5.7)\times10^{10}$ g, which is one order of magnitude higher than the DOC flux from the Pearl River (3.1×10^{10} g C) during the same period. In the winter of 2009, the DIC transported by the CCC to the NSCS was estimated to be $(16.4 \pm 11.3)\times10^{12}$ g (Dai et al., unpublished data), exceeding the DIC flux from the Pearl River (4.7×10^{11} g C) by more than one order of magnitude during the same period. Given that the residence time of seawater on the NSCS shelf is approximately 1–2 years[17,18], the substances transported by the CCC to the NSCS shelf may influence carbonate dynamics over an extended period beyond a single season. However, no study has addressed the cross-seasonal impact of the CCC water, largely due to the difficulty of conducting cross-seasonal field observations. Yang et al.[14] observed high DIC on the NSCS shelf off the Pearl River estuary in May 2011, which may have resulted from the influence of remnant CCC water from the previous winter, driven by the northeast monsoon. Nevertheless, the extent of this remnant CCC influence in spring remains unclear. This study investigates the influence of remnant CCC water transported during the winter driven by the northeast monsoon on the dynamics of the carbonate system on the NSCS shelf off the Pearl River estuary in the spring of 2023. The effect of biological processes and air-sea CO_2 exchanges will also be addressed.

Materials and methods

Study area

The Pearl River is the second largest river in China in terms of freshwater discharge, with an annual runoff of 3.26×10^{11} m^3, 80% of which occurs during the wet season from April to September[19,20]. The Pearl River system comprises three main tributaries, namely the West River, the North River and the East River, as well as several local rivers in the delta. All runoffs from the Pearl River system discharge into the NSCS through eight major outlets via three sub-estuaries: the Lingdingyang, Modaomen, and Huangmaohai.

The Pearl River estuary is located in a tropical climate zone. Generally, a strong northeast monsoon prevails during winter, while relatively weak southwest monsoon dominates during summer. Under the influence of the northeast monsoon, the CCC characterized by high DIC and TA originated from the coastal East China Sea and even the Yellow Sea flows to the NSCS through the Taiwan Strait[12]. In summer, the coastal current reverses its flow direction and becomes substantially weaker[12]. In addition, coastal upwelling occurs along the northeastern coast of the South China Sea under the influence of the southwest monsoon in summer[9,21](Fig. 1).

The freshwater from the Pearl River system forms the Pearl River plume, which flows southwestwardly under the influence of the northeast monsoon, and northeastwardly during the influence of the southwest monsoon[22–25] (Fig. 1). Due to the influence of the Pearl River system, which is characterized by low DIC and TA, both DIC and TA in the surface water on the NSCS shelf exhibit an increasing gradient from the Pearl River estuary offshore[26,27]. In the NSCS, air-sea CO_2 fluxes show pronounced temporal variability, acting as a CO_2 sink in winter, a CO_2 source in summer, with transitions occurring in spring and autumn[28].

Sampling and analysis

Organized by the project "Characterization and Quantification of Critical Points in Planktonic Ecosystems under Multiple Environmental Stresses" supported by the National Key Research and Development Projects of China, a field survey was conducted on the NSCS shelf off the Pear River estuary and northward to the East China Sea shelf in the April 2023. This study focuses solely on the NSCS shelf.

Twelve cross-shelf transects were occupied during April 1–6, 2023 on board the R/V Yanping II (Fig. 1). Temperature, salinity and depth were measured with a Seabird® SBE 917 Conductivity-Temperature-Depth/pressure (CTD) sensor package. Water samples were collected with 12 L Niskin bottles attached to the CTD Rosette. Samples for dissolved oxygen (DO) and carbonate system parameters were collected using Tygon® tubing free of air bubbles. DO samples were taken into 60 mL biological oxygen demand bottles and fixed with Winkler regents[29,30]. Samples for DIC/pH/TA were taken into 250 mL borosilicate bottles with grounded-glass stoppers and poisoned with 250 µL of saturated $HgCl_2$ solution.

DO samples were placed in a constant-temperature water bath (Ningbo Tianheng Instrument Co., Model THYD 0530 W) at 25.00 ± 0.01 ℃ for at least 2 h and measured spectrophotometrically at 466 nm onboard within 4 h of sampling[30,31]. The pH/DIC/TA samples were stored in the dark at room temperature until measurements. pH and DIC were measured simultaneously, and TA was measured within two days after the DIC and pH measurements. DIC was measured at room temperature using a DIC analyzer (Apollo SciTech Model ASC 6 L) with a precision of better than ± 2 µmol kg^{-1}[32]. pH was measured spectrophotometrically at 25 °C using a home-made automatic system integrated with an Agilent 8453 spectrophotometer with a precision of ± 0.0005. The measured pH values were reported on the total hydrogen ion scale at 25 ℃ (hereafter referred to as pH_{25}). TA was determined using a Gran titration method on an automated alkalinity titrator (Apollo SciTech Model AS-ALK3) with a precision of better than ± 2 µmol kg^{-1}, with the temperature maintained constant at 25.00 ± 0.01 ℃ throughout the measurement[30]. Both DIC and TA measurements were calibrated using certified reference material (CRM, batch 207) provided by Dr. Andrew Dickson of the Scripps Institution of Oceanography, with an accuracy of better than ± 2 µmol kg^{-1}. For DIC, CRM calibration was performed every 8 samples. For TA, daily hydrochloric acid calibration was conducted with CRM, and a CRM check was performed every 8–10 samples to ensure the actuary and stability.

During the cruise, surface water partial pressure of CO_2 (pCO_2) was measured continuously. Seawater was pumped continuously from ~ 3 m below the sea surface. CO_2 was continuously measured with a non-dispersive infrared spectrometer (Li-Cor® 7000) after air-water equilibration with a home-made underway system[33]. CO_2 mole fraction (CO_2 fraction hereafter) in the atmosphere was determined every ~ 1–1.5 h. The underway

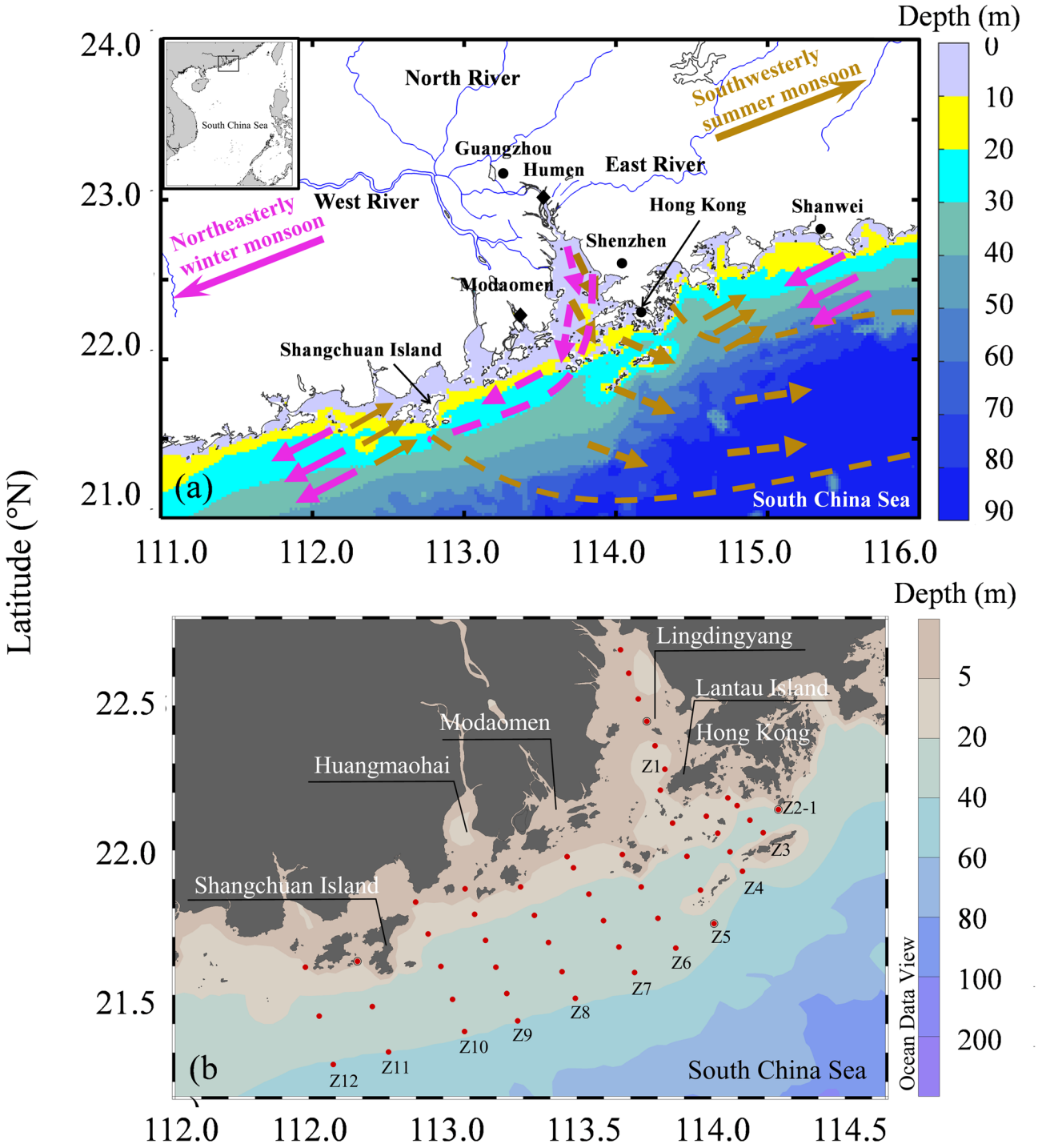

Fig. 1. Geographic map of the Pearl River estuary (**a**) and sampling stations in April 2023 (**b**). In panel (**a**), the inserted map shows the location of the Pearl River estuary; pink dashed and solid arrows indicate the prevailing currents in winter; brown dashed and solid arrows indicate the prevailing currents in summer; the brown dashed line denotes the outer edge of the river plume. In panel (**b**), red dots represent sampling stations; Z1-Z12 indicates the sampling transects. Panel (**a**) was created with software MATLAB (Version 2023B), and the topography and bathymetry data are from the National Centers for Environmental Information (National Oceanic and Atmospheric Administration) at https://www.ncei.noaa.gov/products/etopo-global-relief-model); panel (**b**) was created with ODV (Version 5.6.2) developed by Reiner Schlitzer, available at https://odv.awi.de, 2021.

pCO_2 system was always measuring seawater pCO_2 except during the atmospheric pCO_2 measurement. In situ temperature and salinity were measured with a Seabird SBE 21 SeaCAT thermosalinograph.

The bow intake for atmospheric air sampling was installed ~ 10 m above the sea surface[33]. Wind speed and barometric pressure were measured continuously with a marine meteorological station (Yong 05106) mounted ~ 10 m above the sea surface, with precisions of ± 0.2 m s^{-1} and ± 3 hPa, respectively.

Data processing

pCO_2 and air-sea CO_2 flux calculation

Surface water pCO_2 at the temperature in the equilibrator was calculated from the CO_2 fraction in dry air in the equilibrator and the pressure in the equilibrator after correction for the vapor pressure of water at 100% relative humidity[34]:

$$pCO_2{}^{Eq} = (P_{Eq} - P_{H2O}) \times xCO_2 \tag{1}$$

In the above formula, $pCO_2{}^{Eq}$ is water pCO_2 at the temperature in the equilibrator (µatm); P_{Eq} is pressure in the equilibrator (atm); P_{H2O} is saturated vapor pressure (atm); xCO_2 is the CO_2 mole fraction (µmol mol^{-1}).

pCO_2 in the air was calculated similarly using xCO_2 in the air and the barometric pressure using a formula similar to Formula (1).

Water $pCO_2{}^{Eq}$ obtained from Formula (1) was corrected to pCO_2 at in situ temperature (*in situ* pCO_2, or pCO_2 hereafter, in µatm) using the empirical formula of Takahashi et al.[35].

$$\text{In situ } pCO_2 = pCO_2{}^{Eq} \times \exp\ ((\text{SST-temp}) \times 0.0423) \tag{2}$$

In Formula (2), SST is sea surface temperature (°C); temp is the temperature in the equilibrator (°C).

Net air-sea CO_2 flux (FCO_2 in mmol m^{-2} d^{-1}, positive value indicating CO_2 source) between the surface water and the atmosphere was calculated using the following formula:

$$FCO_2 = k \times 24 \times s \times \rho \times \Delta pCO_2 \times 10^{-5} \tag{3}$$

where k is the CO_2 transfer velocity (cm h^{-1}), which was parameterized using the empirical function of wind speed at 10 m above sea surface (U_{10}); 24 (h d^{-1}) is used to convert the unit of k from cm h^{-1} to cm d^{-1}; s is the solubility of CO_2 (mol kg^{-1} atm^{-1}[36],); ρ is desnity of the seawater (kg m^{-3}[37],); ΔpCO_2 is the pCO_2 difference between the surface water and the atmosphere (µatm). Parameterization of k with U_{10} suggested by Sweeney et al. (2017) and Wanninkhof[38] are most commonly used formulae, with Wanninkhof[38] 7% lower than that of Sweeney et al. (2017). As this little difference has very little influence on the resulting DIC change, Sweeney et al.[39] parameterization was adopted in this study.

Calculations of AOU and excess DIC

Apparent oxygen utility (AOU) is defined as the difference between saturated oxygen concentration (DO_{sat}) and the observed DO, the former of which was calculated according to the formula of Benson and Krause[40].

$$AOU = DO_{sat} - DO \tag{4}$$

The DO saturation (in %) was defined as the ratio of observed DO to the saturated DO.

$$\text{DO saturation} = \frac{DO_{obs}}{DO_{sat}} \times 100\% \tag{5}$$

Excess DIC was defined as the difference between the observed DIC and DIC_{eq} following[41].

$$\text{Excess DIC} = DIC - DIC_{eq} \tag{6}$$

DIC_{eq} is defined as the DIC concentration at air-sea CO_2 equilibrium, and was calculated from TA and atmospheric pCO_2 using the CO2SYS program[42]. The dissolution constants of carbonic acid were from Millero et al.[43]. The CO_2 solubility coefficient was from Weiss[36] and the sulfate dissociation constant from Dickson[44]. The average atmospheric pCO_2 of 409 µatm was used in the calculations.

Estimations of non-conservative DIC changes

The Pearl River estuary and the adjacent NSCS is a three end-member mixing system regulated by physical mixing, air-sea CO_2 exchange and biogeochemical processes[8,45]. To distinguish the influence of biogeochemical processes and air-sea CO_2 exchange on DIC from those of physical mixing, a three-end-member mixing model was adopted to simulate the conservative mixing[45]. Firstly, TA and potential temperature (θ) were used as conservative tracers to estimate the water fractions (f) of the three end-members following[8,45].

$$f_1 + f_2 + f_3 = 1 \tag{7}$$

$$\theta_1 \times f_1 + \theta_2 \times f_2 + \theta_3 \times f_3 = \theta \tag{8}$$

$$TA_1 \times f + TA_2 \times f_2 + TA_3 \times f_3 = TA \tag{9}$$

In the above equations, the subscripts "1", "2," and "3" denote the water masses.

Using the above equations, water fractions can be resolved. Subsequently, conservative mixing values for DIC (DIC_{cons}) and PO_4^{3-} ($PO_4^{3-}{}_{cons}$) can be calculated by multiplying the end-member DIC and PO_4^{3-} concentrations by the respective water fractions (Eqs. 10 and 11). Finally, the non-conservative changes (Δ) in DIC and PO_4^{3-} resulting from biogeochemical processes and air-sea CO_2 exchange can be calculated using Formulae 12 and 13, where a positive value indicates addition and a negative value indicates removal. The PO_4^{3-} data are from Yang et al. (unpublished data).

$$DIC_{cons} = DIC_1 \times f_1 + DIC_2 \times f_2 + DIC_3 \times f_3 \tag{10}$$

$$PO_4^{3-}{}_{cons} = PO_4^{3-}{}_1 \times f_1 + PO_4^{3-}{}_2 \times f_2 + PO_4^{3-}{}_3 \times f_3 \tag{11}$$

$$\Delta DIC = DIC - DIC_{cons} \tag{12}$$

$$\Delta PO_4^{3-} = PO_4^{3-} - PO_4^{3-}{}_{cons} \tag{13}$$

Sensitivity analysis

The reliability of the calculations depend on the accuracy of the end-member values. Due to solar radiation, sea surface temperature exhibits diurnal fluctuation, which may introduce errors into the above estimations. These potential errors can be quantified. As shown in Eqs. 7–13, the error (ε) in the non-conservative change (Δ) depends on the variability in potential temperature (θ_1, θ_2, θ_3), TA (TA_1, TA_2, TA_3) and DIC (DIC_1, DIC_2, DIC_3) of each end-member. Consequently, the error in Δ can be expressed as a function of these variables:

$$f = (\theta_1, \theta_2, \theta_3, TA_1, TA_2, TA_3, DIC_1, DIC_2, DIC_3) \tag{14}$$

Using the error propagation formula[46], it can be obtained:

$$\epsilon_{\Delta DIC} = \frac{1}{n} \times \sqrt{\sum_i^n \left(\begin{array}{c} \left(\frac{\partial (f)}{\partial ([\theta_1]_i)} \times \delta \left([\theta_1]_i\right)\right)^2 + \left(\frac{\partial (f)}{\partial ([\theta_2]_i)} \times \delta \left([\theta_2]_i\right)\right)^2 + \\ \left(\frac{\partial (f)}{\partial ([\theta_3]_i)} \times \delta \left([\theta_3]_i\right)\right)^2 + \left(\frac{\partial (f)}{\partial ([TA_1]_i)} \times \delta \left([TA_1]_i\right)\right)^2 + \\ \left(\frac{\partial (f)}{\partial ([TA_2]_i)} \times \delta \left([TA_2]_i\right)\right)^2 + \left(\frac{\partial (f)}{\partial ([TA_3]_i)} \times \delta \left([TA_3]_i\right)\right)^2 + \\ \left(\frac{\partial (f)}{\partial ([DIC_1]_i)} \times \delta \left([DIC_1]_i\right)\right)^2 + \left(\frac{\partial (f)}{\partial ([DIC_2]_i)} \times \delta \left([DIC_2]_i\right)\right)^2 \\ + \left(\frac{\partial (f)}{\partial ([DIC_3]_i)} \times \delta \left([DIC_3]_i\right)\right)^2 \end{array} \right)} \tag{15}$$

In the above formula, δ is the uncertainty of each parameter of each end-member; n is the number of data.

Based on hourly average sea surface temperature data from the Zhelang Observation Station (https://mds.nmdis.org.cn/), located off the coast of Shanwei City, during the sampling period, the daily fluctuation range of sea surface temperature was calculated to be ± 0.4 °C. This value is comparable to ± 0.7 °C range of sea surface temperature variation observed in the South China Sea basin by Dai et al.[47]. Assuming a temperature fluctuation of ± 0.7 °C and taking uncertainties in DIC and TA as the standard deviations shown in Table 1, the associated error in ΔDIC (εΔDIC) was calculated to be 2.7 μmol kg^{-1}, which is similar to the DIC measurement uncertainty of ±2.0 μmol kg^{-1}. Therefore, the diurnal fluctuation in sea surface temperature has only a minor influence on the error in the calculated DIC, and thus does not significantly affect the results.

End-member selection

Station Z1-1, the most upstream station in Lingdingyang, was selected as the low-salinity Pearl River estuarine water (PRE), characterized by low salinity, low temperature, low DIC and low TA. The average of bottom water from four stations off Huangmaohai (the most inshore stations along sections Z9, Z10, Z11 and Z12) was adopted as the inshore bottom water (BOT) end-member, which is characterized by low temperature, relatively high salinity, relatively low TA, and high DIC. The average of surface water from offshore stations along section Z5, Z6, Z7 and Z9 with salinity > 34.0 was used as the offshore surface water (OSW) end-member, characterized by high temperature, high salinity, high TA, and low DIC. Averages from four stations in the Taiwan Strait (not shown on the sampling station map) during the April 2023 cruise were adopted as the Coastal China Current

End-member	Temperature (°C)	Salinity	TA (μmol kg^{-1})	DIC (μmol kg^{-1})	PO_4^{3-} (μmol kg^{-1})
PRE	21.6	20.8	2064.9	1969.7	1.02
BOT	22.0 ± 0.1	31.2 ± 0.8	2191.4 ± 10.6	2006.3 ± 8.1	0.50 ± 0.06
OSW	24.0 ± 0.2	34.1 ± 0.1	2245.7 ± 3.6	1968.0 ± 3.2	0.04
CCC	19.8 ± 2.2	33.9 ± 0.4	2254.1 ± 6.7	2010.6 ± 33.5	0.14 ± 0.09

Table 1. Potential end-member values of temperature, salinity, TA, DIC and PO_4^{3-} for the Pearl River estuarine water (PRE), inshore subsurface water (BOT), offshore surface water (OSW) and China Coastal Current water (CCC).

(CCC) water end-member values, which are presented in Table 1. The salinity-normalized DIC (NDIC) during the April 2023 cruise (1957.1 μmol kg^{-1}) is very close to that observed in winter (1958.6 μmol kg^{-1} in December 2008; Dai et al. unpublished data). Therefore, the stations selected in April 2023 effectively represent the CCC end-member in winter.

Quantification of the influences of biogeochemical processes and air-sea CO_2 exchange on DIC

The influence of air-sea CO_2 exchange The DIC change due to air-sea CO_2 exchange (ΔDIC_{a-s}) can be calculated from the air-sea CO_2 flux, mixed depth and the duration time[48]:

$$\Delta\,\mathrm{DIC_{a-s}} = FCO_2 \times \frac{\Delta t}{\rho \times H} \tag{16}$$

In the above equations, ΔDIC_{a-s} is the DIC change resulting from air-sea CO_2 exchange (relative to air-sea CO_2 equilibrium). Δt is the time period of air-sea CO_2 exchange; H is the mixed layer depth; ρ is the seawater density.

The influence of biological processes As nitrogen has more complex processes, ΔPO_4^{3-} and Redfield stoichiometry were adopted to calculate the influence of biological processes on DIC (ΔDIC_{bio}, relative to conservative mixing), which can be calculated using the following formula (Redfield et al. 1958).

$$\Delta\,\mathrm{DIC_{bio}} = 106\Delta\,\mathrm{PO_4^{3-}} \tag{17}$$

Results

Hydrological and meteorological background

In the spring of 2023, the Pearl River drainage basin experienced very dry conditions. In March and April 2023, the monthly average freshwater discharge of the Pearl River were 2250 and 4110 $m^3\ s^{-1}$, respectively, equivalent to approximately 47% and 60% of the long-term monthly average (4750 and 6810 and $m^3\ s^{-1}$ during 1998–2022, Fig. 2) (*Hydrological Information Annual Report*, 1998–2022, Ministry of Water Resources, PR China, http://www.mwr.gov.cn/.). The dry Hydrological condition may have influenced the carbonate system dynamics on the NSCS shelf.

Based on meteorological observations from the Waglan Island station of the Hong Kong Observatory, prevailing winds during the cruise (April 1–6, 2023) alternated northeast and southeast directions, with an average wind speeds 7.7±1.0 m s^{-1} (Fig. 3) (wind speed and direction data are from the Hong Kong Observatory at https://www.weather.gov.hk/sc/cis/climat.htm).

Distributions of temperature and salinity

The horizontal distributions of temperature and salinity in the Pearl River estuary exhibited pronounced spatial variabilities. In the surface waters, temperature ranged from 21.2 to 24.6 °C (Fig. 4, a-1). Overall, temperature

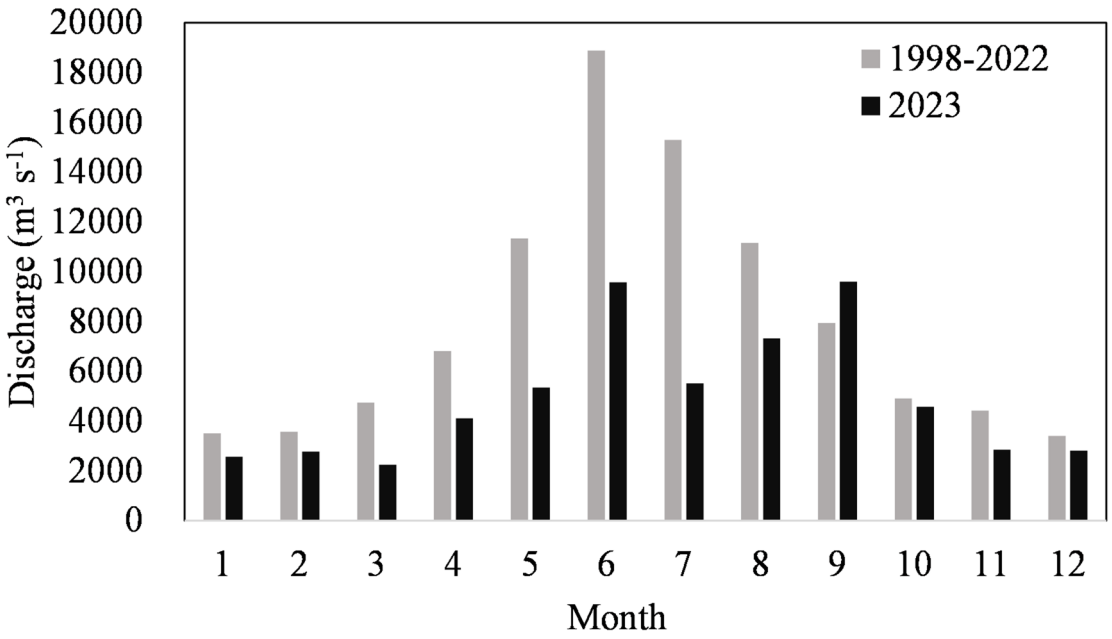

Fig. 2. Freshwater discharge from the three main tributaries (the West River, North River and East Rivers) of the Pearl River system. Data for the lower West, North and East Rivers come from the Wuzhou, Shijiao and Boluo gauge stations, respectively. Data are sourced from the *Hydrological Information Annual Report* (1998–2022), Ministry of Water Resources, PR China, http://www.mwr.gov.cn/.

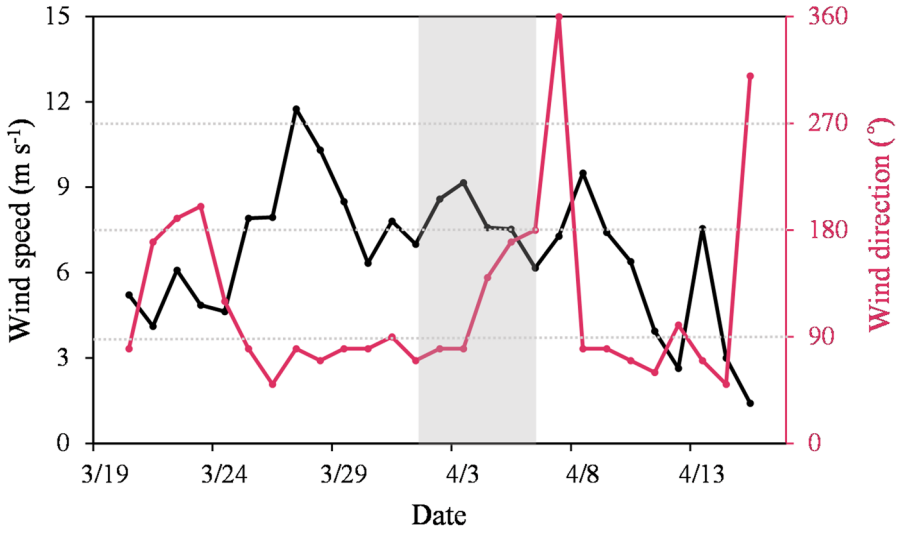

Fig. 3. Time-series variation of wind speed and wind direction at Waglan Island, Hong Kong, during the spring of 2023. The gray shaded area indicates the cruise period. Data are from the Hong Kong Observatory (https://www.weather.gov.hk/sc/cis/climat.htm). The alternating dashed-dotted lines divide the wind direction into four quadrants, representing northeasterly, southeasterly, southwesterly and northwesterly winds from bottom to top, respectively.

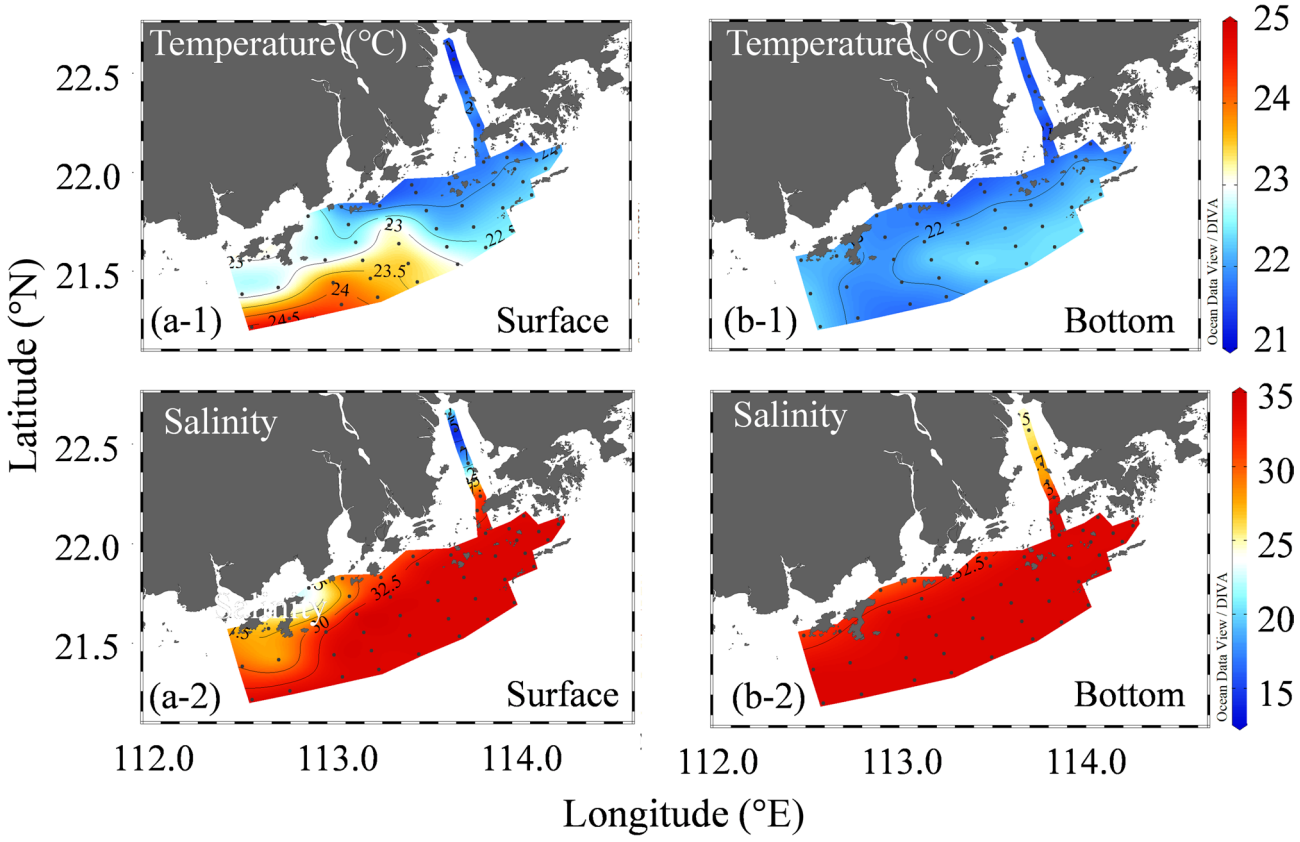

Fig. 4. Spatial distributions of temperature and salinity in surface and bottom waters of the Pearl River estuary and the adjacent northern South China Sea shelf in April 2023. Black dots indicates sampling stations, and thin black lines represent contours of the respective parameters. In the salinity panels, thick black lines denote the contour of salinity 32.

increased from the estuary (Lingdingyang) toward the offshore area. Along the coast, temperature showed an increasing trend from northeast to southwest. Surface water salinity ranged from 25.4 to 34.3. Lowest salinity (< 30) was in the estuary. In the coastal zone, salinity was lower (< 32) along the southwestern coast and higher (> 34) in the southeastern offshore area (Fig. 4a-2). Due to low freshwater discharge, the influence of Pearl River freshwater on the surface water was considerably smaller than in summer[8,27].

In the bottom water, the spatial variabilities of both temperature and salinity were much smaller than those observed in the surface layer. Temperature ranged from 21.5 to 22.4 °C. Low temperatures were in the northeastern area, and high temperatures were observed in the southeastern area (Fig. 4, b-1). Bottom salinity ranged from 25.4 to 34.2, and low salinities were found in the estuary and along the southwestern coast, whereas high salinities occurred in the offshore area (Fig. 4, b-2).

Distributions of carbonate parameters and DO in the water column

Surface water

In surface water, DIC range was 1926.9–2009.8 μmol kg^{-1}. Due to the input of low-DIC Pearl River water, DIC in the surface water in the Lingdingyang generally remained < 1970 μmol kg^{-1}. High DIC values (> 1980 μmol kg^{-1}) were observed along the coast, while low DIC values (< 1970 μmol kg^{-1}) were found in the offshore area (Fig. 5a-1). Horizontally, the average DIC in the inshore water (the two most inshore stations in all transects) was 20.9±8.8 μmol kg^{-1} higher than in the offshore water (salinity > 34.2).

Surface TA ranged from 1995 to 2255 μmol kg^{-1}. The spatial distribution of surface TA was similar to that of salinity, with low TA values (< 2200 μmol kg^{-1}) observed in the estuary and along the northwestern coast, and high TA values (> 2230 μmol kg^{-1}) in the southeast offshore zone (Fig. 5b-1). The low values were likely influenced by the input of low-TA freshwater from the Pearl River. Surface pH_{25} ranged from 7.68 to 8.02 and exhibited a pattern opposite to that of DIC, with low pH_{25} occurring in the inshore high-DIC coastal zone (Fig. 5c-1).

Surface DO concentration ranged from 188.7 to 237.0 μmol kg^{-1}. Relatively low DO values (200.0–210.0 μmol kg^{-1}) were observed along the western coast, whereas high DO values (225.0–230.0 μmol kg^{-1}) were found in the central offshore area (Fig. 5, d-1).

Bottom water

In bottom water, DIC ranged from 1936.8 to 2017.2 μmol kg^{-1}, with the lowest values observed in the estuary. High DIC along the northwestern coast were also present on the shelf, though this feature was less pronounced than in surface water (Fig. 5a-2).

Bottom TA ranged from 2027 to 2256 μmol kg^{-1}, and exhibited a spatial pattern similar to that of surface water (Fig. 5b-2). pH_{25} ranged from 7.74 to 8.01, and its spatial distribution was also comparable to that in surface water (Fig. 5c-2).

DO concentration ranged from 185.9 to 223.0 μmol kg^{-1}, showing a pattern opposite to that of DIC, with low DO along the western coast and high DO in the southeastern offshore zone (Fig. 5d-2). Compared to surface water, bottom DO was relatively lower.

Relationship of DIC and TA with salinity

Figure 6 illustrates the relationships of potential temperature, TA and DIC with salinity on the NSCS shelf (data in the estuary were excluded to focus on the processes on the shelf). In surface waters, potential temperature was relatively homogeneous, with some were even lower than in subsurface and bottom waters (Fig. 6a).

TA generally increased with salinity; however, some values in the low-salinity region were relatively high, approaching or slightly below those in offshore waters. In the subsurface and bottom waters, TA values were similar to those in surface offshore water (Fig. 6b).

DIC showed no clear relationship with salinity. Contrary to the typical pattern increasing DIC with salinity, DIC in the low-salinity zone was higher than that in the high-salinity offshore zone (Fig. 6c).

Surface water pCO_2 and air-sea CO_2 fluxes

Surface water pCO_2 ranged from 369 to 986 μatm, with an average of 448 μatm. High pCO_2 values (> 500 μatm) were observed in the estuary and inshore zones. Two centers of very high pCO_2 (> 600 μatm) were identified: one in the estuary and the other in the area off Modaomen, where the lowest salinities were recorded. In contrast, the offshore area, particularly the southeastern zone, exhibited low pCO_2 values of < 400 μatm. Atmospheric pCO_2 ranged from 406 to 411 μatm. Consequently, the inner estuary (Lingdingyang) and the inshore area acted as CO_2 sources, whereas the southeastern offshore area functioned as a CO_2 sink during the cruise.

The spatial distribution of FCO_2 was similar to that of the surface water pCO_2. FCO_2 ranged from −8.8 to 165.7 mmol m^{-2} d^{-1}, with highest FCO_2 values observed in the inner estuary. On the shelf, the inshore area was generally a weak to moderate source (FCO_2 >4 mmol m^{-2} d^{-1}), except for the area off Modaomen, which was a strong CO_2 source (FCO_2 >40 mmol m^{-2} d^{-1}). In contrast, the southeastern offshore area acted as a weak CO_2 sink of 2–7 mmol m^{-2} d^{-1} (Fig. 7). The average FCO_2 over the entire surveyed area was 3.7±11.1 mmol m^{-2} d^{-1}.

Discussion

Cross-seasonal influence of the winter China Coastal Current water on spring carbonate system

The inner NSCS shelf was typically influenced by the Pearl River water, inshore subsurface water and offshore surface water, exhibiting a distribution pattern characterized by low DIC inshore and high DIC offshore[8,27]. However, during our cruise, much higher DIC was observed in the inshore area than offshore, a phenomenon rarely, if ever, reported in this region. Since DIC concentration in surface water was higher than those in bottom

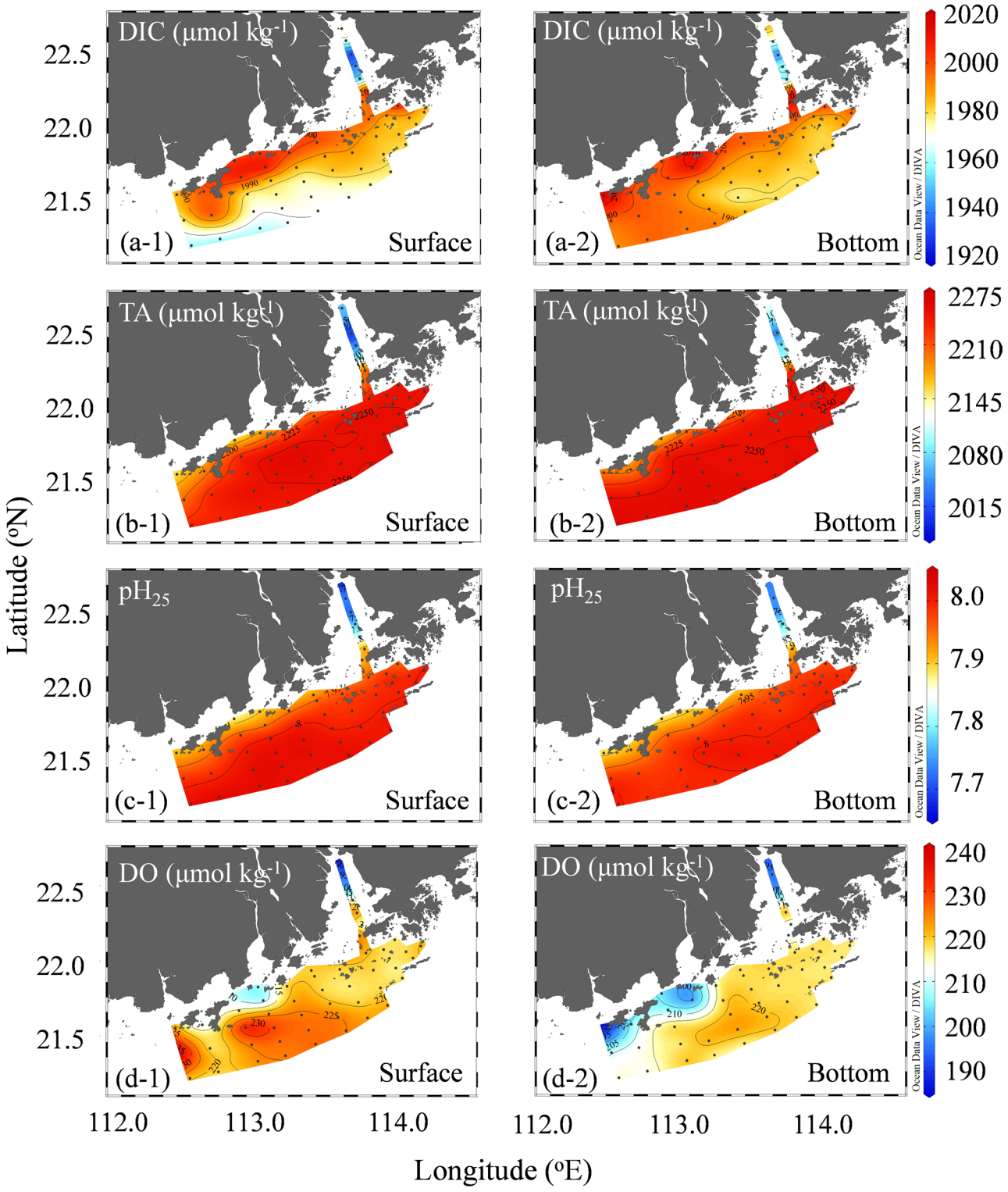

Fig. 5. Spatial distributions of DIC, TA, pH_{25} (pH at 25 °C) and DO in the surface and bottom waters of the Pearl River estuary and adjacent northern South China Sea shelf in April 2023. Black dots indicate sampling stations, and thin black lines represent contours of the respective parameters.

water in the inshore area (Fig. 5a-2 and b-2), the elevated DIC along the coast is unlikely to have originated from the sediment. The potential influence of sediment release can be roughly estimated. In the absence of benthic DIC flux observation for this region, we used the benthic DIC flux data in the northern Gulf of Mexico as a proxy. Assuming a benthic DIC flux of 1.15 mmol m^{-2} d^{-1}[49] and a mixed layer of 24 m during the cruise, the benthic contribution to water column DIC would be 2.8–4.2 μmol kg^{-1} over a water residence time of 60–90

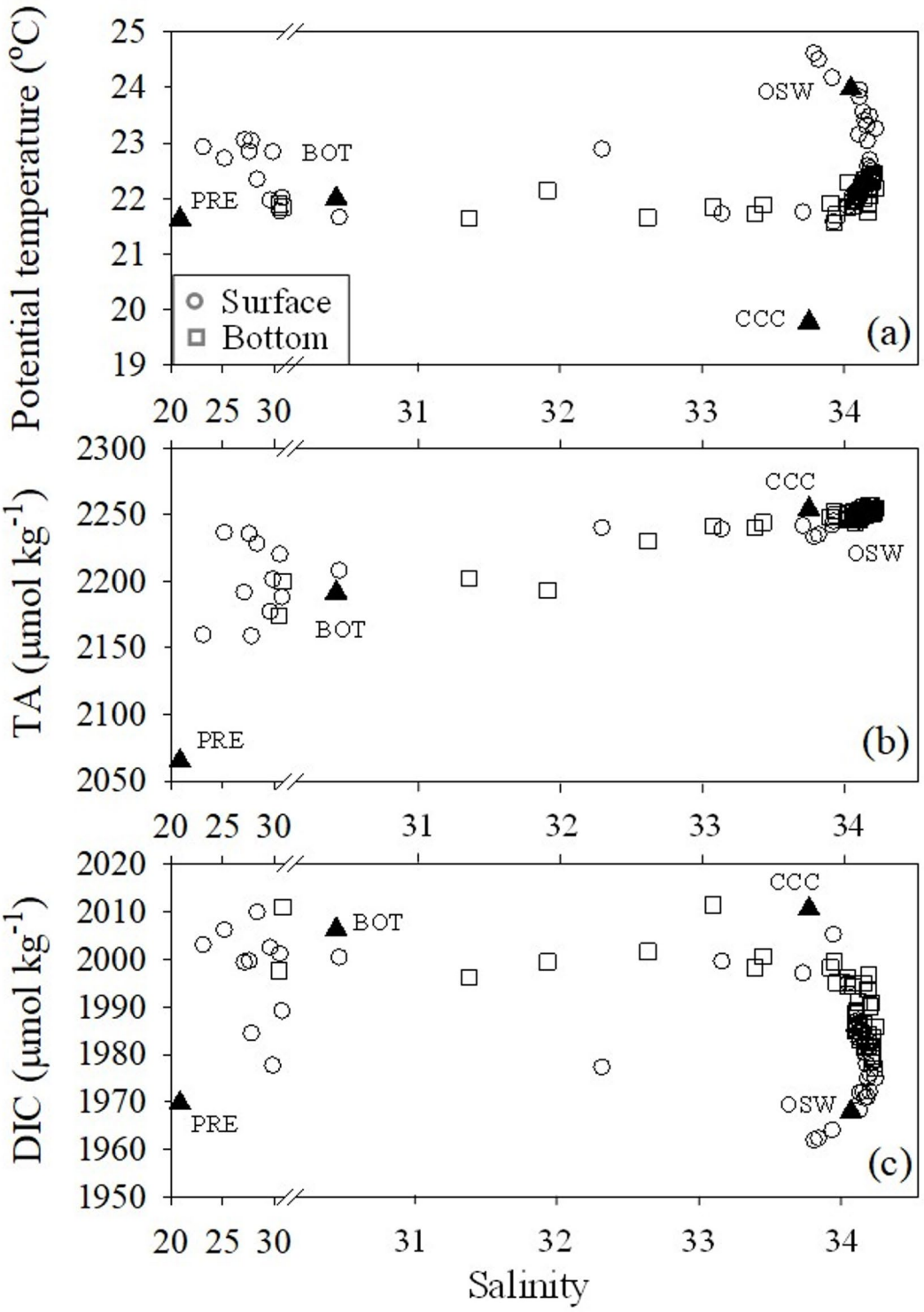

Fig. 6. Relationships of potential temperature (**a**), TA (**b**) and DIC (**c**) with salinity in the study area in April 2023. Solid triangles denote the potential end-members: Pearl River estuarine water (PRE), inshore bottom water (BOT), offshore surface water (OSW) and China Coastal Current water (CCC).

days. This estimate suggest that benthic input is not the primary source of the elevated coastal DIC observed in surface waters.

Given the strong China Coastal Current, driven by the northeast monsoon, transports a large volume of high-DIC water to the NSCS, and given the relatively long water residence time of the upper layer in the NSCS (approximately 1–3 years[50]), the cross-seasonal influence of the remnant winter CCC water— originating from the coastal East China Sea (and even the Yellow Sea) and characterized by high-DIC— is a plausible explanation

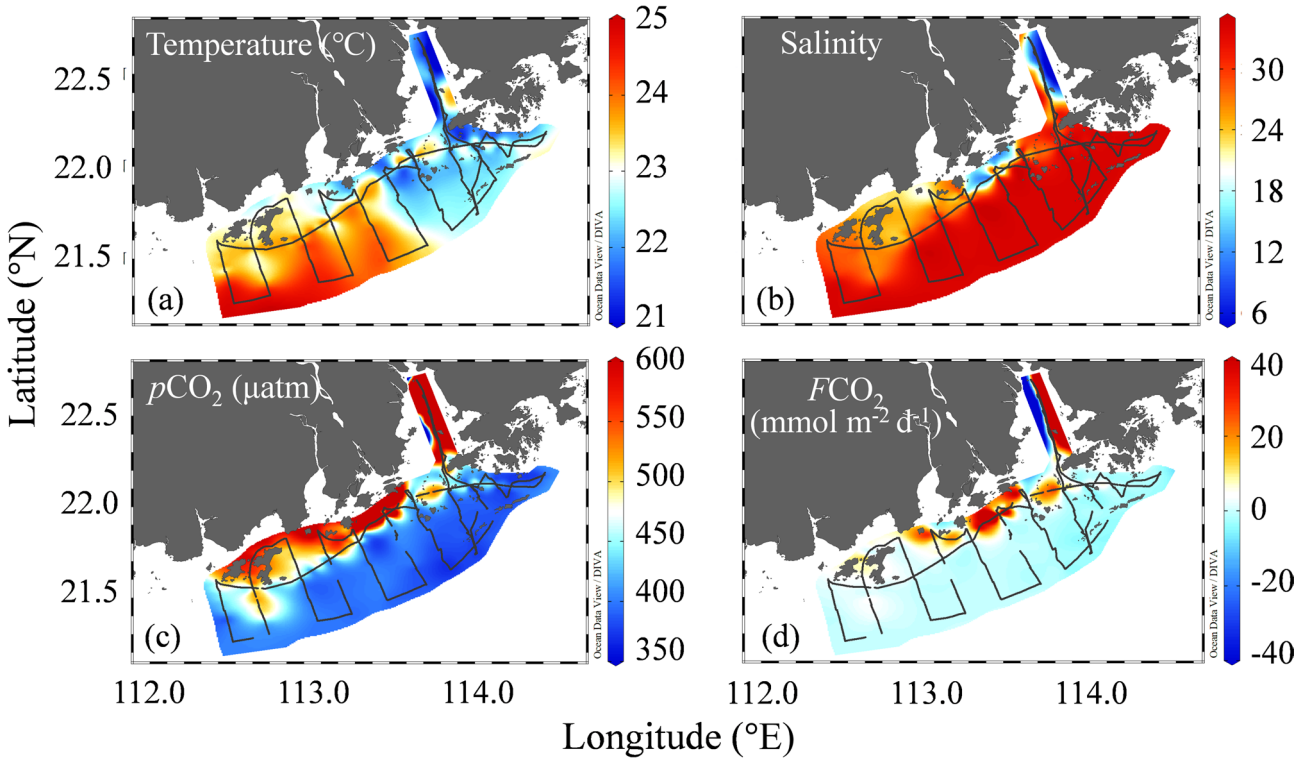

Fig. 7. Spatial distributions of temperature, salinity, partial pressure of CO_2 (pCO_2) and air-sea CO_2 flux (FCO_2) of surface waters in the Pearl River estuary and adjacent northern South China Sea shelf in April 2023. Dotted lines indicate the cruise tracks.

for the elevated DIC observed in inshore waters. This explanation is consistent with the regional circulation pattern, wherein the northeast monsoon drives alongshore transport and limits cross-shelf exchange[51].

In this section, we examine the influence of remnant winter CCC water on the spring carbonate system using end-member mixing models. Three scenarios are tested, (1) the typical three end-member mixing of Pear River estuarine water (PRE), the inshore bottom water (BOT) and offshore surface water (OSW); (2) four end-member mixing of PRE, BOT, OSW and remnant CCC water; and (3) three end-member mixing of BOT, OSW and remnant CCC water. By comparing the estimated mixing results with observation, a reasonable scenario—namely, the influence of remnant CCC water—was confirmed.

Mixing scenario of PRE, BOT and OSW

In the first scenario, mixing among PRE, BOT and OSW was assumed. The calculated water fractions of PRE were < 0.5 across the surveyed area, with high values occurring in the western inshore and offshore regions (Fig. 8a). BOT fraction exceeded 0.7 in the eastern half of the surveyed area and fell < 0.3 in the western area (Fig. 8b). OSW fraction were < 0.2 in the eastern area and > 0.7 in the southwestern offshore area. Although the spatial distribution of the OSW fractions appeared reasonable, the BOT fraction seemed unusual.

The calculated conservative DIC showed high values in the eastern area and low values in the western area (Fig. 8d), a pattern completely different from the observed DIC distribution, which was characterized by high values inshore and low values offshore, Fig. 8e). An apparent "DIC removal" of up to 40 µmol kg^{-1} was estimated in the eastern area, where observed DO saturation ranged from 80% to 103% (where slight DIC addition would be expected). In contrast, an apparent "DIC addition" of up to 20 µmol kg^{-1} was found in the southwestern area, where observed DO saturation was 105–108% (where slight DIC removal would be expected) (Fig. 8f). The stark mismatch between the calculated conservative DIC and the observed DIC along with the DIC "addition" or "removal" patterns that contradict oceanographic principles, suggests that the selected end-members in this scenario are likely unreasonable.

Mixing scenario of PRE, BOT, OSW and CCC

The temperature, salinity, and carbonate parameters of the CCC observed during the cruise were highly consistent with the findings reported by Yang et al.[14]. As mentioned above, remnant CCC water transported from the coastal East China Sea in winter may influence the NSCS shelf in spring. Therefore, CCC end-member was added to the conservative mixing calculation, resulting a four end-members mixing scenario (PRE, BOT, OSW and CCC), with salinity, potential temperature and TA used as conservative tracers.

The calculated conservatively mixed DIC showed high values (> 1990 µmol kg^{-1}) in the eastern and low values (< 1970 µmol kg^{-1}) in the western areas (Fig. 9a), a pattern again entirely different from the spatial distribution of

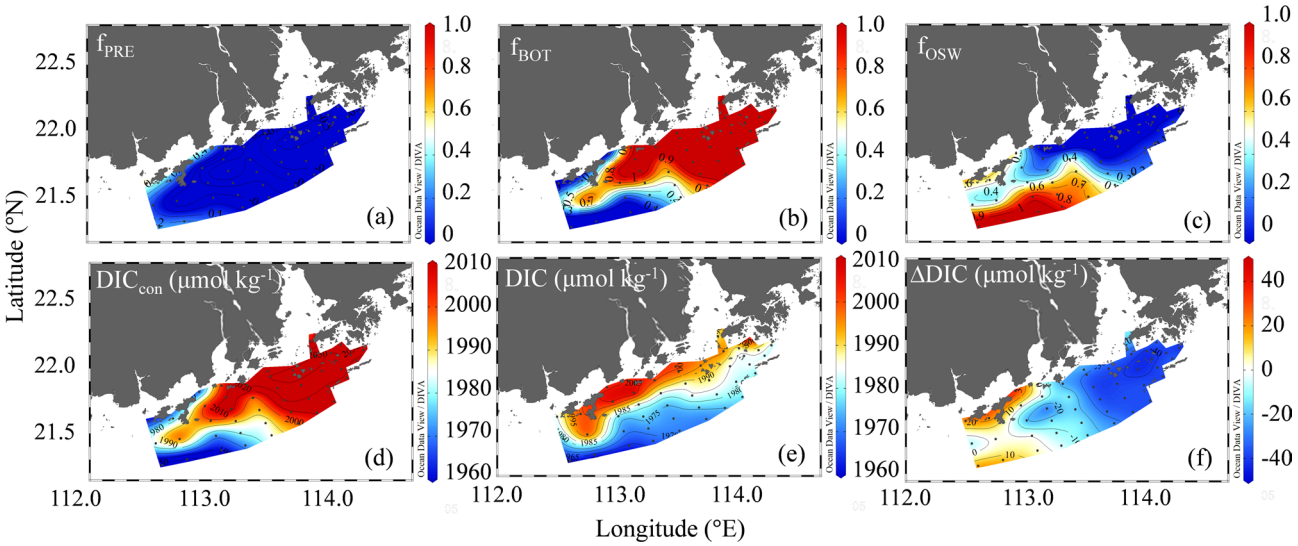

Fig. 8. Water fractions of the three end-member mixing scenario involving the Pear River estuarine water (f_{PRE}, **a**), inshore bottom water (f_{BOT}, **b**) and offshore surface water (f_{OSW}, **c**); and spatial distributions of estimated conservatively mixed DIC (DIC_{cons}, **d**), observed DIC (DIC, **e**) and DIC non-conservative DIC change (ΔDIC, **f**) in surface water in April 2023. Black dotes denote the sampling stations.

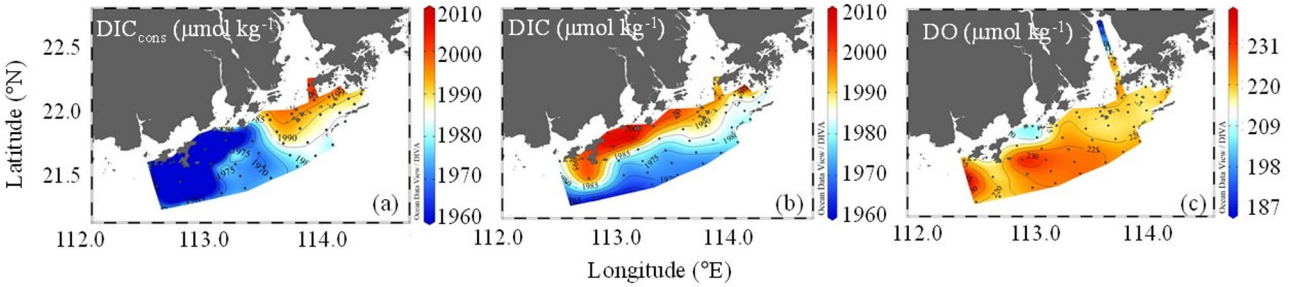

Fig. 9. Spatial distribution of estimated conservative DIC (DIC_{cons}, **a**) under the mixing scenario of four end-member (PRE, OSW, BOT and CCC), along with observed DIC (DIC, **b**) and observed DO (**c**) in surface water in the spring of April 2023. Black dotes indicate sampling stations.

observed DIC (Fig. 9b). This result also conflicts with oceanographic principles when considered in relation to DO distribution, suggesting that the selection of end-members in this scenario remains unreasonable.

Mixing scenario of BOT, OSW and CCC

The average water discharge during the two weeks prior to the cruise (the water travel time from the gauge station to the NSCS shelf[8], was only 2200 $m^3\ s^{-1}$, which is even lower than the long-term (1998–2022) monthly winter average of 3500 $m^3\ s^{-1}$ (Ministry of Water Resources, PR China, http://www.mwr.gov.cn/). Low salinity water (< 30) was confined to the estuary. The DIC concentration in the Pearl River water during the dry season is 2000 μmol kg^{-1}[52]. When mixed with offshore seawater (salinity = 34.1, DIC = 1968.0 μmol kg^{-1}), the resulting DIC at salinity 30 would be 1971.8 μmol kg^{-1}, a value very close to the DIC concentration in offshore seawater. Therefore, the influence of Pearl River water on DIC over the NSCS shelf was almost invisible. Accordingly, the PRE end-member was removed, and a three end-member mixing scenario involving BOT, OSW and CCC was calculated. The results indicate that the northwestern part of the surveyed area was influenced by CCC water and OSW, the inshore area was dominated by BOT water, and the southeastern offshore water was dominated by OSW (Fig. 10).

The spatial distribution of conservatively mixed DIC was consistent with observed DIC, showing high values inshore (> 1985 μmol kg^{-1}) and low values offshore. In most areas, the non-conservative change in DIC was near zero, indicating that carbonate parameters of the surface water were primarily regulated by water mixing (Fig. 10).

The end-member mixing model simulations demonstrate that remnant CCC water, transported to the NSCS shelf by the winter monsoon played a critical role in shaping the carbonate system distribution along the coast during the spring of 2023. Typical DIC in offshore surface water (offshore stations with salinity > 34.2) ranged from 1970.8 to 1982.7 μmol kg^{-1}, with an average of 1976.6±4.0 μmol kg^{-1}. In contrast, DIC in the coastal zone

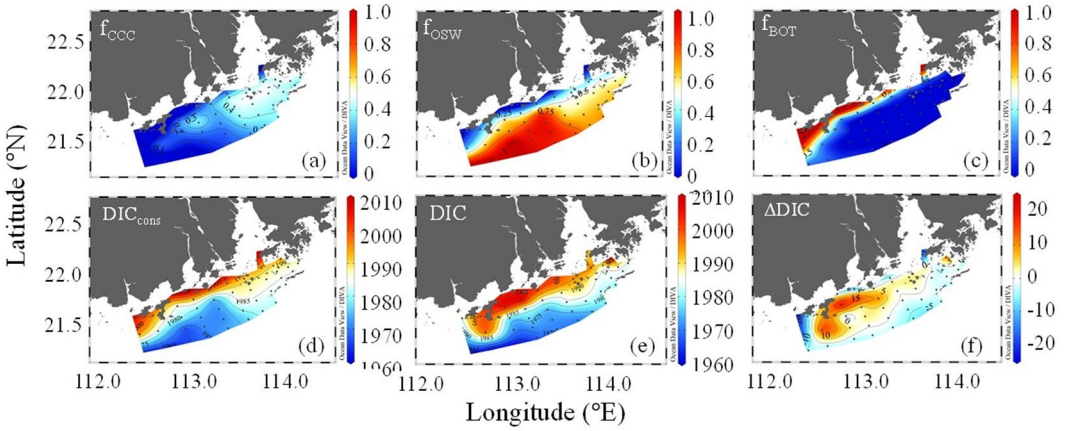

Fig. 10. Water fractions of the end-members (f_{CCC}, f_{OSW} and f_{BOT}, **a**–**c**), and spatial distributions of estimated conservative DIC (DIC_{cons}, **d**), observed DIC (DIC, **e**), and non-conservative DIC change (ΔDIC, **f**) in the surface water in the April 2023 under the three end-member mixing scenario involving inshore bottom water (BOT), offshore surface water (OSW) and China Coastal Current (CCC) water. Concentrations units are μmol kg^{-1}.

(the two nearshore stations in each transect) ranged from 1982.6 to 2009.8 μmol kg^{-1}, averaging 1997.6±7.7 μmol kg^{-1}. Mixing with the remnant CCC water thus elevated DIC in the coastal water.

Qualitative analysis of biogeochemical processes affecting DIC

Overall, DIC addition (Δ > 0) was observed in the northwestern inshore area, referred to hereafter the inshore high-DIC region. In contrast, the southeastern offshore region exhibited DIC removal (Δ < 0) and is termed the offshore low-DIC region in the following section.

The relationship between excess DIC and AOU across the entire surveyed area was generally consistent with the Redfield ratio (ΔC: $-\Delta O_2$=106:138 = 0.77) (Fig. 11a). However, the relationship of in the inshore high-DIC region differed markedly from that in the offshore low-DIC region. In the offshore low-DIC region, both excess DIC and AOU were predominately negative (Fig. 11b), indicating that the dominating biological process was photosynthesis, which consumes DIC and produces O_2. Moreover, the excess DIC to AOU ratio (ΔC: $-\Delta O_2$ = 0.85) was higher than the Redfield ratio, suggesting the influence of other processes. This indicates lower O_2 production relative to the DIC removal compared with the Redfield stoichiometry, implying the influences of air-sea CO_2 and O_2 exchange. O_2 reaches air-sea equilibrium more quickly than CO_2[53]; that is O_2 is released from seawater to the atmosphere more quickly, weakening the negative AOU values. This interpretation is supported by a comparison of air-sea CO_2 and O_2 fluxes (Fig. 11c): the O_2 flux (FO_2) was positive, while the CO_2 flux (FCO_2) was negative, and FO_2 (~ 10.8 mmol m^{-2} d^{-1}) was substantially larger than the absolute value of FCO_2 (0.5 mmol m^{-2} d^{-1}). Therefore, air-sea exchanges played important role influencing DIC in the water column.

Regarding the relationship between the excess DIC and AOU in the inshore high-DIC region, at stations where both excess DIC and AOU were negative (Fig. 11b), O_2 flux was positive, while CO_2 flux was negative. This phenomenon might be attributed to the fact that O_2 reached air-sea equilibrium faster than CO_2, reduces the absolute value of AOU (negative). It may also be related to the rapid turnover of marine-derived organic matter produced by photosynthesis, further reducing the absolute value of negative excess DIC[27,54].

At stations where both excess DIC and AOU were positive (Fig. 11b), DIC was likely regulated by organic matter remineralization. The ratio of excess DIC to AOU was lowers than the Redfield stoichiometry, indicating that multiple processes regulated non-conservative DIC in this region: O_2 entered seawater from the atmosphere (FO_2 was negative), while CO_2 escaped from seawater to the atmosphere (FCO_2 was positive), causing deviation from the Redfield stoichiometry. Additionally, this pattern could be influenced by terrestrial organic matter or by diatoms producing high-nitrogen organic matter (increased C: N ratio) under nitrate–depleted conditions, which consumes more O_2 while releasing less CO_2 (smaller ΔDIC).

At stations where excess DIC was negative but AOU was positive (Fig. 11b), organic matter remineralization may have occurred. The difference in air-sea equilibration times between CO_2 and O_2 led a decoupling of excess DIC and AOU.

It should be noted that, in addition to sea-air CO_2 exchange and photosynthesis/remineralization, processes such as nitrification, denitrification, carbonate mineral reactions may also cause deviations of the ΔDIC–AOU relationship from the Redfield stoichiometry. However, during the cruise, DO concertation was high (> 180 μmol kg^{-1}), suggesting that denitrification was likely unimportant. Furthermore, the aragonite saturation state (Ω_{arag}) was consistently > 1, and no sharp Ω_{arag} anomalies corresponding to deviations in TA were detected, indicating that calcium carbonate precipitation or dissolution had no discernible influence. In summary, the biogeochemical processes regulating the spatial distribution of the carbonate system in the inshore high-DIC region and offshore low-DIC region were primarily driven by the relative contributions of biological processes and sea-air gas exchange, which will be quantified below.

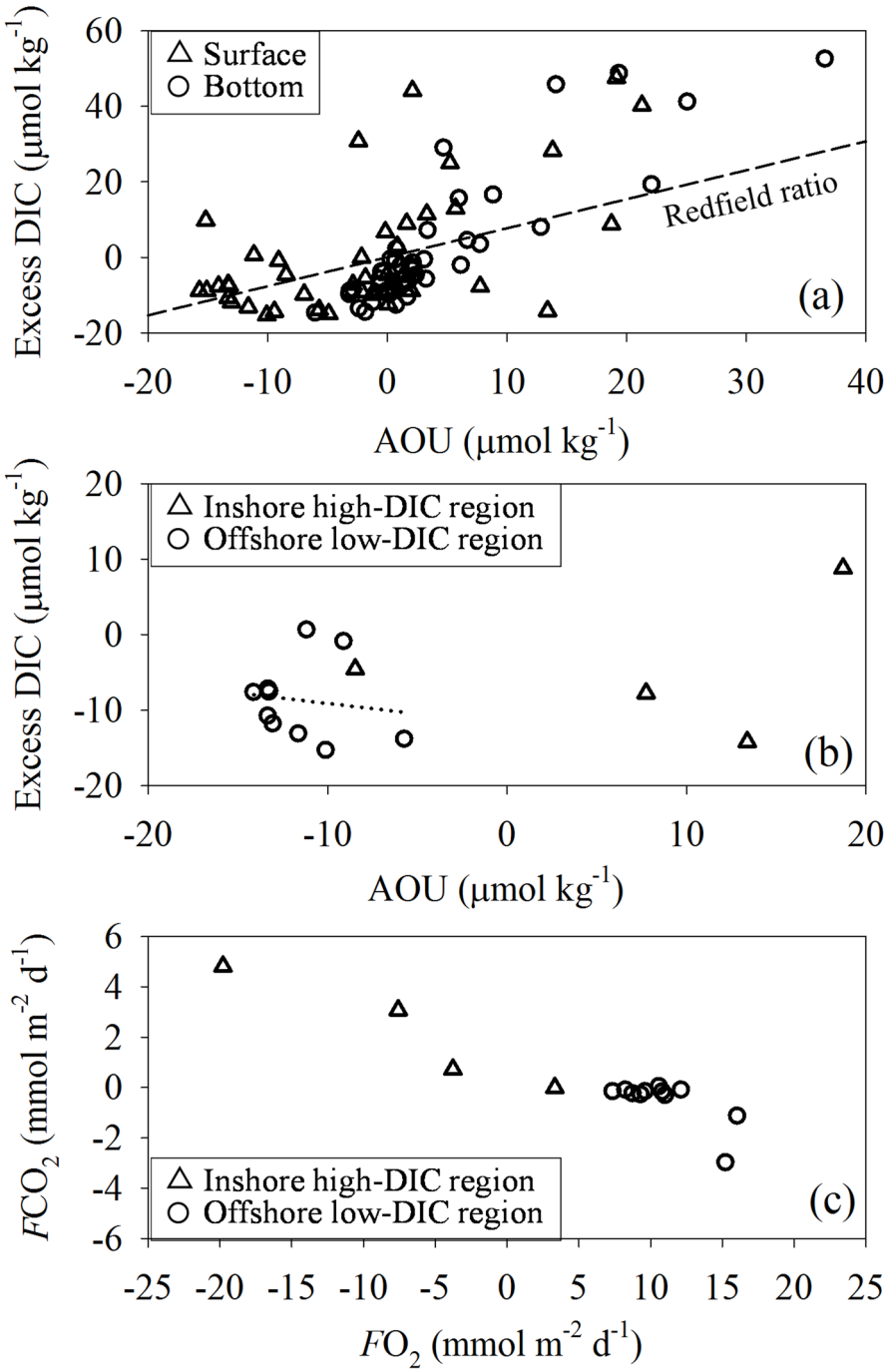

Fig. 11. Relationship of excess DIC with AOU for all station data (**a**), Excess DIC with AOU for surface water in the inshore high-DIC region and offshore low-DIC region (**b**), and air-sea CO_2 fluxes (FCO_2) with air-sea O_2 fluxes (FO_2) in surface waters (**c**) in the study area in April 2023. The dotted line in panel (**b**) represents linear regression line of excess DIC and AOU for the offshore low-DIC region based on a Type II linear regression ($y = -0.852x - 20.744$, $R^2 = 0.5049$, $p = 0.03193$).

Contributions of biogeochemical processes and air-sea CO_2 exchange to DIC changes

The non-conservative DIC change (ΔDIC) in surface waters of the inshore high-DIC region was 16.7 ± 4.1 μmol kg^{-1}, indicating DIC addition, while that in the offshore low-DIC region was -1.8 ± 3.3 μmol kg^{-1}, indicating DIC removal. Below, the influences of biogeochemical processes and air-sea CO_2 exchange on DIC are quantified for these two typical regions.

According to Redfield stoichiometry, the ratio of DIC change to PO_4^{3-} change during photosynthesis or aerobic respiration is 106[55–57]. Based on the observed change in PO_4^{3-}, organic matter remineralization would

Region	Season	MLD (m)	Surface water pCO_2 (μatm)	Atmospheric pCO_2 (μatm)	Wind speed (m s^{-1})	FCO_2 (mmol m^{-2} d^{-1})
Inshore high-DIC region	Winter	11.3	356 ± 24	389	8.1	−4.60 ± 3.38
	Spring	6.0	491 ± 53	412	3.0 ± 0.83	2.15 ± 1.91
Offshore low-DIC region	Winter	22.7	327 ± 24	389	8.1	−8.66 ± 3.33
	Spring	9.1	397 ± 10	412	3.7 ± 0.92	−0.52 ± 0.84

Table 2. Surface water and atmospheric pCO_2, mixed layer depth (MLD), wind speed and air-sea CO_2 fluxes (FCO_2) in the inshore high-DIC and offshore low-DIC regions.

increase DIC by 11.6 ± 3.0 μmol kg^{-1} in the inshore high-DIC region, whereas photosynthesis would decrease DIC by 5.1 ± 3.5 μmol kg^{-1} in the offshore low-DIC region.

Under typical sea conditions, the air-sea CO_2 equilibration timescale ranges from several tens to several hundred days. Therefore, the cross-seasonal cumulative effects of air-sea CO_2 exchange on water column DIC must be considered.

The study area acts a CO_2 sink in winter[28]. March is a transitional period from a CO_2 sink to CO_2 source, with the CO_2 sink period lasting until mid-March and the source period beginning after mid-March[28]. As CO_2 absorbed during the previous "sink period" also affects water DIC in spring, a 23-day period (from February 20 to March 14) was included to account for the influence of air-sea CO_2 exchange during the sink phase. A 23-day period (from March 15 to April 6) was adopted as the CO_2 "source period".

Mixed layer depth is a necessary parameter for calculating of the influence of air-sea CO_2 exchange on the water DIC. In this study, mixed layer depth was defined as the depth at which surface density differs by 0.03 kg m^{-3}[58–60].

FCO_2 during the CO_2 "sink period" was calculated using $pCO_2$from Li et al.[28]. FCO_2 was − 4.60 ± 3.38 mmol m^{-2} d^{-1} in the inshore high-DIC region and − 8.66 ± 3.33 mmol m^{-2} d^{-1} in the offshore low-DIC region (Table 2). For the CO_2 "source period", the average FCO_2 during the cruise was adopted. During this period, FCO_2 values were 2.15 ± 1.91 mmol m^{-2} d^{-1}in the inshore high-DIC region and − 0.52 ± 0.84 mmol m^{-2} d^{-1} in the offshore low-DIC region. Although uncertainties may rise from using pCO_2 data of Li et al.[28], the calculated FCO_2 patterns remain consistent with our interpretation. In the inshore high-DIC region, air-sea CO_2 exchange during the CO_2 "sink period" increased DIC by 9.2 ± 6.7 μmol kg^{-1}, whereas it decreased DIC by 8.1±7.2 μmol kg^{-1} during the CO_2 "source period". The cumulative effect of air-sea CO_2 exchange resulted in a net DIC increase of 1.1±7.0 μmol kg^{-1} in this region. In the offshore low-DIC region, air-sea CO_2 exchange increased DIC by 8.6±3.3 μmol kg^{-1} during the CO_2 "sink period" and by 1.3±2.1 μmol kg^{-1} during the CO_2 "source period". The cumulative effect led to a net DIC increase of 9.9±2.8 μmol kg^{-1} in the offshore low-DIC region (Fig. 12).

In the inshore high-DIC region, biological processes and air-sea CO_2 exchange together increased DIC by 12.7 ± 7.6 μmol kg^{-1}, which is consistent with the non-conservative DIC change of 16.7 ± 4.1 μmol kg^{-1} (Fig. 12). In the offshore low-DIC region, biological processes and air-sea CO_2 exchange jointly increased DIC by 4.7 ± 4.4 μmol kg^{-1}. According to the end-member mixing model, the non-conservative DIC change in this region was − 1.8 ± 3.30 μmol kg^{-1}. Although the two values (4.7 ± 4.4 μmol kg^{-1} and − 1.8 ± 3.3 μmol kg^{-1}) are not identical, they are considered comparable given the DIC measurement error of ± 2 μmol kg^{-1}. A conceptual diagram of the influencing processes is shown in Fig. 13.

Concluding remarks

In April 2023, a field survey was conducted in the Pearl River estuary and the adjacent NSCS shelf to investigate the carbonate system dynamics. Contrary to the typical DIC distribution pattern observed in large river-dominated coasts (where DIC increases offshore), DIC in the inshore zone was high (up to > 1980 μmol kg^{-1}) compared to the offshore area (< 1970 μmol kg^{-1}), with average DIC in coastal surface waters being 20.9±8.8 μmol kg^{-1} higher than in offshore surface waters. Mixing of residual high-DIC winter China Coastal Current water dominated the DIC distribution pattern. In addition, biological processes and air-sea CO_2 exchange also played important roles. In the inshore high-DIC region, biological processes and air-sea CO_2 exchange increased DIC by 11.6±3.0 and 1.1±7.0 μmol kg^{-1}, respectively, with a combined effect of 12.7 ± 7.6 μmol kg^{-1}. In the offshore low-DIC region, biological processes decreased DIC by 5.1 ± 3.5 μmol kg^{-1}, while air-sea CO_2 exchange increased DIC by 9.9±2.8 μmol kg^{-1}, resulting a net increase of 4.7 ± 4.4 μmol kg^{-1}. This study highlights the cross-seasonal (or longer-term) influence of costal current water on the carbonate system in coastal regions.

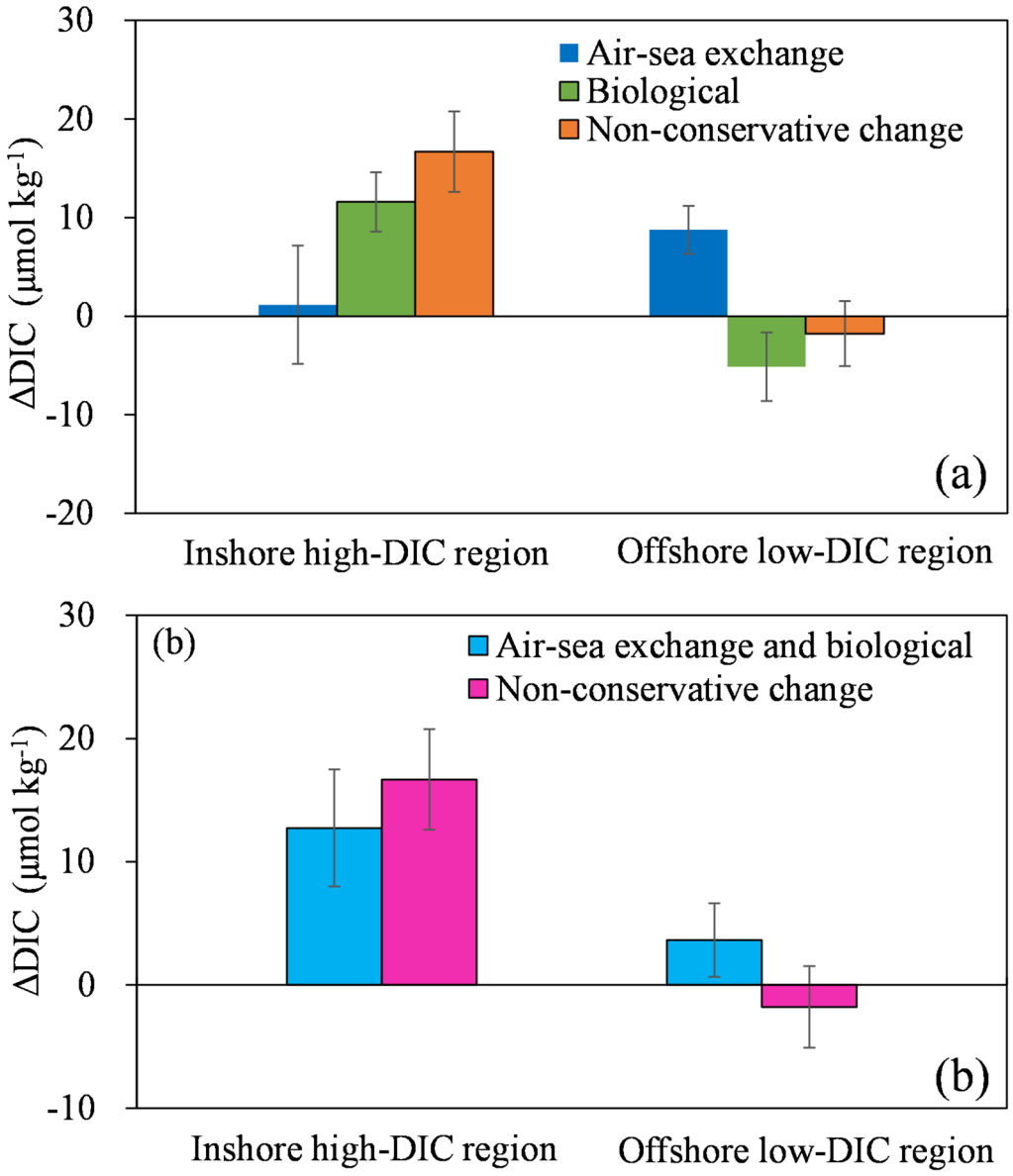

Fig. 12. DIC change (ΔDIC) due to air-sea CO_2 exchange (air-sea exchange), biological effects (biological), and comparison with the estimated non-conservative DIC change in surface water in the two typical regions. Error bars represent standard deviations. In panel (**b**), "air-sea exchange and biological" denotes the sum of DIC changes from air-sea CO_2 exchange and biological processes.

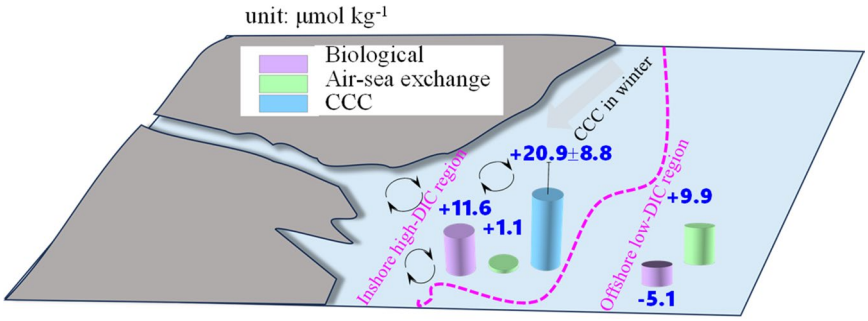

Fig. 13. Conceptual model of the contribution of various processes to DIC change in the surface water of the coast off the Pearl River estuary in April 2023.

Data availability

The data used in this study (DIC, TA. pH and DO) in the NSCS off the Pearl River estuary in April 2023) are available at Science Data Bank (https://www.scidb.cn/en) with DIO# 10.57760/sciencedb.37693.

Received: 4 January 2026; Accepted: 22 May 2026
Published online: 02 June 2026

References

1. Amann, T., Weiss, A. & Hartmann, J. Inorganic carbon fluxes in the inner Elbe Estuary, Germany. *Estuaries Coasts* **38**, 192–210 (2014).
2. Bauer, J.E., Cai, W.-J., Raymond, P. A. et al. The changing carbon cycle of the coastal ocean. *Nature* **504**(7478), 61–70 (2013).
3. Chen, C. A. et al. Air-sea exchanges of CO_2 in the world's coastal seas. *Biogeosciences* **10**, 6509–6544 (2013).
4. Cai, W.-J. Estuarine and coastal ocean carbon paradox: CO_2 sinks or sites of terrestrial carbon incineration?. *Annu. Rev. Mar. Sci.* **3**, 123–45 (2011).
5. Dai, M, J. Su, Y. Zhao, et al. 2022. Carbon fluxes in the coastal ocean: synthesis, boundary processes, and future trends. *Annu. Rev. Earth Planet. Sci.* **50**, 593–626 (2022).
6. Gattuso, J. P., Frankignoulle, M. & Wollast, R. Carbon and carbonate metabolism in coastal aquatic ecosystems. *Annu. Rev. Ecol. Syst.* **29**, 405–434 (1998).
7. Regnier, P. et al. Modelling estuarine biogeochemical dynamics: from the local to the global scale. *Aquat. Geochem.* **19**, 591–626 (2014).
8. Cao, Z. et al. Dynamics of the carbonate system in a large continental shelf system under the influence of both a river plume and coastal upwelling. *J. Geophys. Res.* **116**, G02010 (2011).
9. Gan, J. et al. Interaction of a river plume with coastal upwelling in the northeastern South China Sea. *Cont. Shelf Res.* **29**, 728–740 (2009).
10. Guo, X. et al. Seasonal variability and future projection of ocean acidification on the East China Sea Shelf off the Changjiang Estuary. *Front. Mar. Sci.* **8**, (2021).
11. Han, A. et al. Inter-shelf nutrient transport from the East China Sea as a major nutrient source supporting winter primary production on the northeast South China Sea shelf. *Biogeosciences* **10**, 8159–8170 (2013).
12. Jan, S. et al. Seasonal variation of the circulation in the Taiwan Strait. *J. Mar. Syst.* **35**, 249–268 (2002).
13. Pan, A. et al. Response characteristics and mechanisms of the Zhejiang-Fujian coastal current off Pingtan Island to the relaxation of the winter monsoon in 2006 [J]. *Sci. China Earth Sci.* **42**, 1317–1328 (2012) ((**in Chinese with English abstract**)).
14. Yang, W. et al. Seasonal dynamics of the carbonate system under complex circulation schemes on a large continental shelf: The northern South China Sea. *Prog. Oceanogr.* **197**, (2021).
15. Zhang, C., Huang, Y. & Ding, W. Enhancement of Zhe-Min coastal water in the Taiwan Strait in winter. *J. Oceanogr.* **76**, 197–209 (2020).
16. Meng, F. et al. Seasonal dynamics of dissolved organic carbon under complex circulation schemes on a large continental shelf: The Northern South China Sea. *J. Geophys. Res. Oceans* **122**, 9415–9428 (2017).
17. Liu, K. K. et al. *Carbon and nutrient fluxes in continental margins* 464–482 (Springer, 2010).
18. Yang, S., Lee, D. & Ho, T. The isotopic composition of cadmium in the water column of the South China Sea. *Geochim. Cosmochim. Acta* **98**, 66–77 (2012).
19. Dai, M. et al. *Physical dynamics and biogeochemistry of the Pearl River plume: Biogeochemical dynamics at large river–coastal interfaces* 321–352 (Cambridge University Press, 2012).
20. Zhao, H. T. *Evolution of the Pearl River estuary* 357th edn. (Ocean Press, 1990) ((**in Chinese**)).
21. Gan, J. et al. Intensified upwelling over a widened shelf in the northeastern South China Sea. *J. Geophys. Res. Oceans* **114**(C9), C09019 (2009).
22. Dong, L. et al. Seasonal variation and dynamics of the Pearl River plume. *Continent. Shelf Res.* **24**, 1761–1777.
23. Ou, S., Zhang, H. & Wang, D. Dynamics of the buoyant plume off the Pearl River Estuary in summer. *Environ. Fluid Mech.* **9**, 471–492 (2009).
24. Su, J. Overview of the South China Sea circulation and its influence on the coastal physical oceanography outside the Pearl River Estuary. *Continent. Shelf Res.* **24**, 1745–1760 (2004).
25. Wong, L., Chen, J. & Dong, L. A model of the plume front of the Pearl River Estuary, China and adjacent coastal waters in the winter dry season. *Continent. Shelf Res.* **24**, 1779–1795 (2004).

26. Su, J. et al. Tracing the origin of the oxygen consuming organic matter in the hypoxic zone in a large eutrophic estuary: The lower reach of the Pearl River Estuary, China. *Biogeosciences* **14**, 4085–4099 (2017).
27. Zhao, Y. et al. Dynamics of inorganic carbon and pH in a large subtropical continental shelf system: Interaction between eutrophication, hypoxia, and ocean acidification. *Limnol. Oceanogr.* **65**(6), 1359–1379 (2020).
28. Li, Q. et al. Partial pressure of CO_2 and air-sea CO_2 fluxes in the South China Sea: Synthesis of an 18-year dataset. *Prog. Oceanogr.* **182**, (2020).
29. Carpenter, J. H. The Chesapeake Bay Institute technique for the Winkler dissolved oxygen method. *Limnol. Oceanogr.* **10**, 141–143 (1965).
30. Guo, X. et al. Coupling of carbon and oxygen in the Pearl River plume in summer: Upwelling, hypoxia, reoxygenation and enhanced acidification. *J. Geophys. Res. Oceans* **128**, (2023).
31. Labasque, T. et al. Spectrophotometric Winkler determination of dissolved oxygen: Re-examination of critical factors and reliability. *Mar. Chem.* **88**, 53–60 (2004).
32. Cai, W.-J. et al. The biogeochemistry of inorganic carbon and nutrients in the Pearl River estuary and the adjacent Northern South China Sea. *Continent. Shelf Res.* **24**, 1301–1319 (2004).
33. Zhai, W. et al. Seasonal variations of sea–air CO_2 fluxes in the largest tropical marginal sea (South China Sea) based on multiple-year underway measurements. *Biogeosciences* **10**, 7775–7791 (2013).
34. Weiss, R. F. & Price, B. A. Nitrous oxide solubility in water and seawater. *Marine Chem.* **8**, 347–359 (1980).
35. Takahashi, T., Olafsson, J., Goddard, J. G., Chipman, D. W. & Sutherland, S. C. Seasonal variation of CO_2 and nutrients in the high-latitude surface oceans: A comparative study. *Global Biogeochem. Cycles* **7**, 843–878 (1993).
36. Weiss, R. F. Carbon dioxide in water and seawater: the solubility of a non-ideal gas. *Marine Chem.* **2**, 203–215 (1974).
37. Millero, F. J. *Chemical Oceanography* 4th Edition, 227–258 (CRC Press, 2013).
38. Wanninkhof, R. Relationship between wind speed and gas exchange over the ocean. *J. Geophys. Res. Oceans* **97**, 7373–7382 (2002).
39. Sweeney, C. et al. Constraining global air-sea gas exchange for CO_2 with recent bomb ^{14}C measurements. *Global Biogeochem. Cycles* **21**, GB2015 (2007).
40. Benson, B. B. & Krause, J. D. The concentration and isotopic fractionation of oxygen dissolved in freshwater and seawater in equilibrium with the atmosphere. *Limnol. Oceanogr.* **29**, 620–632 (1984).
41. Xu, Y., Pierrot, D. & Cai, W.-J. Ocean carbonate system computation for anoxic waters using an updated CO2SYS program. *Marine Chem.* **195**, 90–93 (2017).
42. Pierrot, D., Lewis, E. & Wallace, D. W. R. *MS Excel Program Developed for CO2 System Calculations* (Carbon Dioxide Information Analysis Center (CDIAC) Oak Ridge National Laboratory, U.S. Department of Energy, 2006).
43. Millero, F. J. Carbonate constants for estuarine waters. *Marine Freshw. Res.* **61**, 139–142 (2010).
44. Dickson, A. G. Standard potential of the reaction $AgCl\,(s) + 1/2H_2(g) = Ag\,(s) + HCl\,(aq)$, and the standard acidity constant of the ion HSO_4^- in synthetic seawater from 273.15K to 318.15K. *Chem. Thermodyn.* **22**, 113–127 (1990).
45. Han, A. et al. Nutrient dynamics and biological consumption in a large continental shelf system under the influence of both a river plume and coastal upwelling. *Limnol. Oceanogr.* **57**, 486–502 (2012).
46. Taylor, J. R. *An introduction to error analysis* 2nd edition, 45–93 (Colorado University Press, 1997).
47. Dai, M, Z. Lu, W. Zhai, et al. 2009. Diurnal variations of surface seawater pCO_2 in contrasting coastal environments. *Limnol. Oceanogr.* **54**, 735–745 (2009).
48. Li, B. et al. Riverine influences and seasonal dynamics: Exploring carbonate system variations and air-sea CO2 fluxes in the Southern Yellow Sea and East China Sea. *J. Geophys. Res. Oceans* **129**, (2024).
49. Cai, W.-J. et al. Preferential dissolution of carbonate shells driven by petroleum seep activity in the Gulf of Mexico. *Earth Planet. Sci. Lett.* **248**, 227–243 (2006).
50. Liu, Z. & Gan, J. Three-dimensional pathways of water masses in the South China Sea: A modeling study. *J. Geophys. Res. Oceans* **122**, 6039–6054 (2017).
51. Jan, S., Sheu, D. D. & Kuo, H. M. Water mass and throughflow transport variability in the Taiwan Strait. *J. Geophys. Res. Oceans* **111**(C12), (2006).
52. Guo, X. H. et al. Inter-annual variability of the carbonate system in the hypoxic upper Pearl River estuary in winter. *Front. Mar. Sci.* **7**, (2020).
53. Zeebe, R. E. & Wolf-Gladrow, D. *CO2 in seawater: Equilibrium, kinetics, isotopes* 80–83 (Elsevier oceanography book series, 2003).
54. Hopkinson, C. S., Vallino, J. J. & Nolin, A. Decomposition of dissolved organic matter from the continental margin. *Deep Sea Res. Part II Top. Stud. Oceanogr.* **49**, 4461–4478 (2002).
55. Dai, M. et al. Why are some marginal seas sources of atmospheric CO_2?. *Geophysical Research Letters* **40**, 2154–2158 (2013).
56. Gruber, N. & Deutsch, C. A. C A. Redfield's evolving legacy. *Nat. Geosci.* **7**, 853–855 (2014).
57. Redfield, A. C. The biological control of chemical factors in the environment. *Am. Sci.* **46**, 205–221 (1958).
58. de Montégut, B. et al. Mixed layer depth over the global ocean: An examination of profile data and a profile-based climatology. *J. Geophys. Res. Oceans* **109**(C12), (2004).
59. Sallée, J. et al. Summertime increases in upper-ocean stratification and mixed-layer depth. *Nature* **591**, 592–598 (2021).
60. Weller, R. A. & Plueddemann, A. J. Observations of the vertical structure of the oceanic boundary layer. *J. Geophys. Res. Oceans* **101**(C4), 8789–8806 (1996).
61. Chen, C. A. Rare northward flow in the Taiwan Strait in winter: a note. *Continent. Shelf Res.* **23**, 387–391 (2003).
62. Chou, W. et al. The carbonate system in the East China Sea in winter. *Mar. Chem.* **123**, 44–55 (2011).
63. Guo, X. & Wong, G. T. F. Carbonate chemistry in the Northern South China Sea Shelf-sea in June 2010. *Deep Sea Res. Part II Top. Stud. Oceanogr.* **117**(SI), 119–130 (2015).

Acknowledgements

Zhaozhang Chen and Longqi Yang organized the CTD sampling and processed the CTD data. We thank the crews of the R/V Yanping II for their assistance during the cruise. Shuqi An is acknowledged for his help in sampling and TA measurements. We are also grateful to the chief scientist, Dr. Hao Zhang, for the help during the cruise.

Author contributions

Shiping Lei and Yi Yang participated the cruise and collected the samples. Yi Yang measured DO, while Shiping Lei and Dezhi Bu measured DIC and pH, Shiping Lei and Xianghui Guo drafted the manuscript; Yan Li, Kuanbo Zhou, Jin-Yu Terence Yang and Zhongyong Gao participated in discussions regarding data interpretation. All co-authors reviewed and revised the manuscript.

Funding

The study was supported by the Natural Science Foundation of China (42141001) and National Key R&D Pro-

jects (2022YFC3105302).

Declarations

Competing interests
The authors declare no competing interests.

Additional information
Supplementary Information The online version contains supplementary material available at https://doi.org/10.1038/s41598-026-55237-x.

Correspondence and requests for materials should be addressed to X.G.

Reprints and permissions information is available at www.nature.com/reprints.

Publisher's note Springer Nature remains neutral with regard to jurisdictional claims in published maps and institutional affiliations.